

DOI: 10.1093/icde/awae091

Advance access publication date: 22 October 2024 Research Article

# Computational analysis of unsteady oscillatory flow of nanofluid with variable electric conductivity: gear-generalized differential quadrature approach

Muhammad Idrees Afridi <sup>10</sup>1,2, Muhammad Sabaoon Khan<sup>3,\*</sup>, Muhammad Qasim<sup>4</sup> and Ali J. Chamkha<sup>5</sup>

### **Abstract**

This study numerically investigated the entropy production in nanofluids' dissipative unsteady oscillatory flow characterized by variable electric conductivity and magnetic heating effects. The imposition of the non-isothermal boundary condition on the oscillatory stretching sheet plays a crucial role in establishing the self-similar solution in the presence of viscous heating. An external magnetic field (uniform in space and time) is imposed perpendicular to the plane of the oscillating stretched boundary. The energy equation, incorporating viscous dissipation effects and momentum equation, is reduced to nonlinear coupled partial differential equations and numerically solved using the Gear-generalized differential quadrature scheme. Additionally, to ensure the precision and reliability of the outcomes, the numerical code undergoes a thorough validation process that involves comparing its outputs to the findings of previous available studies. The Corcione model is implemented to describe the nanofluid's effective viscosity and thermal conductivity. Furthermore, expressions for entropy production and relative irreversibility parameter (Bejan number), considering variable electric conductivity, are derived and computed based on solutions obtained from momentum and energy equations. The impacts of parameters such as magnetic parameter, variable electric conductivity parameter, Eckert number, Strouhal number, Prandtl number and temperature difference parameters on flow, heat transfer, entropy generation, and Bejan number are systematically illustrated and examined. We observed that increasing the variable electric conductivity parameters reduces the velocity profiles while improving the thermal fields. Similar behavior is found when the strength of a magnetic field is increased. The skin friction coefficient exhibits an augmentation in response to the Eckert number, dimensionless time, Strouhal number, nanoparticle volume fraction, magnetic parameter, and variable thermal conductivity parameter. Conversely, the Nusselt number increases concerning the Strouhal number and nanoparticle volume fraction. At the same time, it declines in association with the magnetic parameter, dimensionless time, Eckert number, and variable electric conductivity parameter. This comprehensive investigation enhances our understanding of nanofluid dynamics and provides valuable insights for optimizing thermal management systems across various engineering

**Keywords:** heat transfer, time-dependent flow, viscous dissipation, variable electric conductivity, oscillatory flow, generalized gear differential quadrature method (GGDQM)

## **Nomenclature**

Nom	ienciature	$T^*$ :	Dimensionless temperature [-]
Be:	Bejan number [-]	ŧ:	Dimensional time [sec]
$B_0$ :	Strength of the magnetic field $[Kg^{1/2}m^{-1}sec^{-1/2}\Omega^{1/2}]$	U,V:	Dimensional velocity components [msec-1]
$C_P$ :	Specific heat capacity [m²sec-2 Kelvin-1]	$\bar{X}, \bar{Y}$ :	Dimensional spatial coordinates [m]
Ė‴ :	Volumetric entropy generation rate	ho :	Density [kgm <sup>-3</sup> ]
	[Kg <sup>-1</sup> m <sup>-1</sup> sec <sup>-3</sup> Kelvin <sup>-1</sup> ]	$\sigma$ :	Electrical conductivity $[\Omega^{-1} m^{-1}]$
Ec:	Eckert number [-]	$\mu$ :	Dynamic viscosity [kgm <sup>-1</sup> sec <sup>-1</sup> ]
$H_0$ :	Magnetic Parameter [-]	arphi :	Volume fraction of nanoparticles [-]
k :	Thermal conductivity [Kg.m.sec <sup>-3</sup> Kelvin <sup>-1</sup> ]	au :	Dimensionless time [-]
Ns:	Entropy generation number [-]	Λ:	Variable electrical conductivity parameter [-]
Pr:	Prandtl number [-]	χ:	Temperature ratio parameter [-]
Re:	Reynolds number [-]	Subscripts:	
S:	Strouhal number [-]	bf:	Base fluid
T :	Temperature [Kelvin]	nf:	Nanofluid

<sup>&</sup>lt;sup>1</sup>School of Mathematics and Computer Science, Hanjiang Normal University, Shiyan 442000, China

<sup>&</sup>lt;sup>2</sup>Applied Science Research Center, Applied Science Private University, Amman 11931, Jordan

<sup>&</sup>lt;sup>3</sup>Department of Civil Engineering, Kardan University, Kabul 1007, Afghanistan

<sup>&</sup>lt;sup>4</sup>Department of Mathematics, COMSATS University Islamabad, Islamabad Campus, Park Road, Tarlai Kalan, Islamabad 45550, Pakistan

<sup>&</sup>lt;sup>5</sup>Faculty of Engineering, Kuwait College of Science and Technology, Doha District, 35004, Kuwait

<sup>\*</sup>Correspondence: m.sabaoon@kardan.edu.af

## 1. Introduction

Using fluids as a heat transfer medium covers various applications involving cooling systems, heat exchangers, electronic thermal management, chemical reactions, geothermal heating, and cooling. Heat transfer is critical to any of these processes to ensure optimal performance. Traditional or ordinary fluids such as water, engine oil, and ethylene glycol typically exhibit low thermal conductivity and do not allow for adequate heat transfer. Conventional fluids are enhanced with nano-sized particles, such as oxides, carbides, metals, or carbon nanotubes, which have higher thermal conductivity properties to alleviate such a drawback. Choi (1995) was the first to investigate the convection in nanoparticle-suspended fluids and perform research on their properties. His work was done at the Argonne National Laboratory. He proposed that including nano-sized particles in a base fluid enhances thermal conductivity and improves heat transfer rates. Subsequently, nanofluids have found diverse applications in electronic cooling components, industrial systems, nuclear systems cooling, biomedicine, and other fields (Minkowycz et al., 2012; Subramanian et al., 2019; Hatami & Jing, 2020; Bhanvase & Barai, 2021). Nanofluids are recognized for their enhanced thermophysical properties, which are not solely determined by adding microscopic particles to primary liquids. Instead, these properties depend on factors such as the nanoparticle's shape and size, volume fraction, and characteristics of the base fluid (Noreen et al., 2017; Sheikholeslami & Bhatti, 2017; Saleem et al., 2020; Salehi et al., 2023; Wang et al., 2023).

Entropy generation quantifies the degree of irreversibility inherent in natural processes. When entropy generation occurs, it signifies a decrease in the quality of energy, known as exergy. The primary objective in designing thermal devices is the efficient utilization of energy. This goal is accomplished by minimizing entropy generation within the system. Consequently, in energy optimization challenges and the design of various heat removal engineering systems, minimizing entropy generation or the dissipation of available becomes essential. This involves addressing factors such as heat transfer, fluid friction, and electric conduction, all influenced by the selected design variables under optimization analysis. Bejan (1979) was the first to investigate entropy generation in fluid dynamics. He investigated entropy generation in convective viscous fluid flow within a channel, attributing it to viscous friction and heat transfer within the fluid. He also showed that various factors can contribute to entropy generation in thermal engineering problems, where entropy generation means the loss of available energy for work. Then, Bejan & Kestin (1983) calculated the volumetric rate of entropy production in fluid flow. Many scholars have dealt with the causes of entropy generation in various flow systems and performed parametric studies to reduce entropy production. Here, we highlight a few recent studies for the benefit of our readers (Afridi et al., 2024; Afridi, Chen et al., 2022; Alsabery et al., 2022; Cui et al., 2023; Hussain et al., 2024; Jena & Mishra, 2023; Khan et al., 2018, 2020; Noreen & Qurat Ul Ain, 2019; Qasim et al., 2017; Rafique et al., 2024; Roşca et al., 2024; Sakkaravarthi et al., 2024; Soomro et al., 2017; Zhang et al., 2024) Unsteady fluid dynamics manifest ubiquitously within natural phenomena and various industrial contexts. Such fluid behaviors stem from many causative factors, including impulsive motions or abrupt accelerations of boundaries, the imposition of unsteady forces at boundaries, the inherent fluctuating nature of the flow, and periodic motions of boundaries, among others. Oscillatory flow is an unsteady flow characterized by its periodic nature, wherein fluid particles undergo regular back-and-forth motion between two defined points within the system. The flow generated via oscillation of a stretching sheet was first examined by Wang (2002) who finds numerous engineering and industrial applications like film casting, fiber spinning, thermal barrier coatings, polymer extrusion, drawing, and annealing. The investigation of the boundary layer flow generated from the oscillation of a stretching sheet has captivated researchers' interest. Rajagopal et al. (2006) considered the impact of an oscillatory motion of an electrically conducting viscoelastic fluid over a permeable stretching surface. The effects of velocity and thermal slip on flow over an oscillatory sheet were studied by Abbas et al. (2009). Zheng et al. (2013) investigated the combination of heat and mass transfer in an electrically conducting fluid flowing over an oscillatory stretching sheet by accounting for Soret and Dufour effects. Sheikh & Abbas (2015) scrutinized the impact of heat generation/absorption on a chemically reacting magnetohydrodynamic (MHD) flow, considering the effect of thermophoresis. Ali et al. (2016) conducted a comprehensive investigation to analyze how the presence of a heat sink/source affects the characteristics of heat transfer and flow of a couple of stress fluids. Mkhatshwa et al. (2021) conducted a detailed investigation into an Eyring-Powell fluid's oscillatory mixed convection MHD flow over a stretching sheet attached to a non-Darcian porous medium. The study incorporated several complex phenomena, including chemical reactions and variations in viscosity, thermal conductivity, nonlinear thermal radiation, and temperature-dependent diffusivity properties. In polymer extrusion, the desired mechanical properties of the stretched sheet depend primarily on the cooling rate. The choice of cooling liquid is crucial for achieving the desired properties in the final product, emphasizing the importance of contemplating this aspect in the process. The optimal choice for cooling liquid in these processes is nanofluid. Recently, researchers have explored nanofluids flow over a stretching surface, exploring a variety of base fluids and combinations of nanoparticles (Alharbi, 2024; Cui et al., 2022; Farooq et al., 2024; Ghasemi & Hatami, 2021; Idrees Afridi et al., 2023; Yasir, Khan et al., 2023; Yasir, Malik et al., 2023; Yasir & Khan, 2024).

In this study, we aim to investigate the MHD boundary layer flow of a nanofluid  $(C_2H_6O_2 - TiO_2)$  with temperature-dependent electric conductivity (Adeosun & Ukaegbu, 2022; Adesanya et al., 2023; Makinde & Onyejekwe, 2011; Qasim et al., 2020; Qasim, Ali et al., 2019) over an oscillatory stretching sheet. While previous research has explored various aspects of nanofluid and MHD flow, there is a lack of detailed analysis on how temperature-dependent conductivity impacts the overall flow dynamics and heat transfer efficiency. Moreover, entropy generation analysis of the oscillatory flow induced by the stretching surface has not yet been explored. Therefore, this study fills this gap. These governing equations are first modeled and then simplified under boundary layer assumptions. The differential quadrature method (DQM) (Afridi, Ashraf et al., 2022; Ashraf et al., 2020; Qasim, Afridi et al., 2019; Thumma et al., 2020; Wakif et al., 2019) is employed to compute the numerical solutions for these self-similar equations, a method widely adopted by researchers to tackle such type of problems. In DQM, partial differential equations (PDEs) are firstly transformed into systems of ordinary differential equations (ODEs) through discretization by approximating derivatives using discrete points, often chosen with quadrature rules like Gauss-Lobatto points. Partial derivatives with respect to spatial variables are replaced with algebraic equations involving function values at specific grid points. Standard numerical approaches, such as Runge-Kutta methods or iterative solvers, can solve the system of coupled ODEs. In this study, we used the Gear technique, a multistep method incorporating

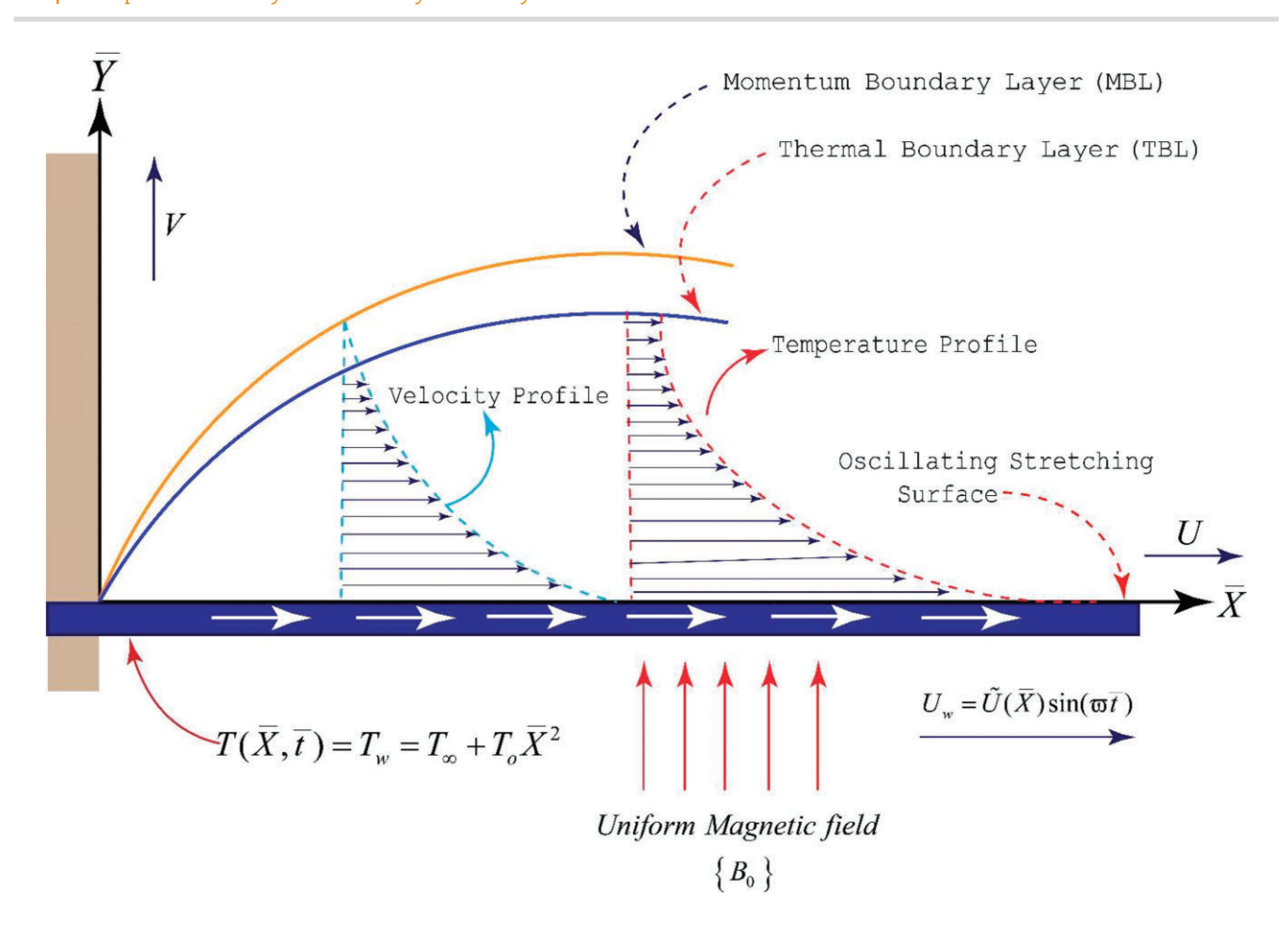


Figure 1: Flow configuration with coordinates axes.

**Table 1:** Thermophysical properties of the nanofluidic mixture  $TiO_2(s) - C_2H_6O_2(bf)$ .

Thermophysical properties	Expressions
Density (Wakif et al., 2021; Wakif, Boulahia, Mishra et al., 2018) (Wakif, Boulahia, Ali et al., 2018)	$ ho_{nf}=(1-arphi) ho_{bf}+arphi ho_{ ext{ iny S}}$
Specific Heat Capacity (Wakif et al., 2021; Wakif, Boulahia, Mishra, et al., 2018) (Wakif, Boulahia, Ali, et al., 2018)	$\left(C_{p} ight)_{nf} = rac{\left(1-arphi ight) ho\left( hoC_{P} ight)_{bf} + arphi\left( hoC_{P} ight)_{S}}{\left(1-arphi ight) ho_{bf} + arphi ho_{S}}$
Dynamic Viscosity (Corcione, 2011)	$\begin{cases} \mu_{nf} = \frac{\mu_{bf}}{1 - \frac{34.87}{d_s^{0.3}} \left[ \frac{6M(C_2 H_6 O_2)}{N_{A\nu} \pi \rho_{bf_0}} \right]^{0.1} \varphi^{1.03}, & \rho_{bf_0} = 1115 kg.m^{-3}, \\ M(C_2 H_6 O_2) = 62 \times 10^{-3} kg.mol^{-1}, & N_{A\nu} = 6.022 \times 10^{23} mol^{-1} \end{cases}$
Thermal Conductivity (Corcione, 2011)	$\begin{cases} k_{nf} = \left[1 + 4.4 \left[\frac{2K_B \rho_{bf} T}{\pi \mu_{bf}^2 d_s}\right]^{0.4} Pr^{0.66} \left(\frac{T}{T_{Fr}}\right)^{10} \left(\frac{k_s}{k_{bf}}\right)^{0.03} \phi^{0.66}\right] k_{bf}, \\ T \approx T_{\infty} = 300K, \ K_B = 1.38066 \times 10^{-23} J.K^{-1}, \ T_{Fr} = 260.65K \end{cases}$

 $\textbf{Table 2:} \ \ \textbf{Thermophysical properties of } \{\textbf{TiO}_2(s), \textbf{C}_2\textbf{H}_6\textbf{O}_2(bf)\} \ \ \textbf{(Gholinia et al., 2018; Nayak et al., 2020; Zhang et al., 2023)}.$ 

Physical mear	nings	Mixture constituents		
Thermophysical properties	Symbols/Units	TiO <sub>2</sub> (s)	$C_2H_6O_2(bf)$	
Equivalent diameter	d(nm)	40	0.56 077 995	
Density	$\rho(kgm^{-3})$	4250	1114.4	
Specific heat capacity	$C_P(Jkq^{-1}K^{-1})$	686.2	2415	
Thermal conductivity	$k(Wm^{-1}K^{-1})$	8.9538	0.252	
Electrical conductivity	$\sigma(\Omega^{-1}m^{-1})$	$6.27 \times 10^{-5}$	$1.07 \times 10^{-4}$	
Dynamic viscosity	$\mu(\times 10^{-5} \text{Pas})$	_	1570	

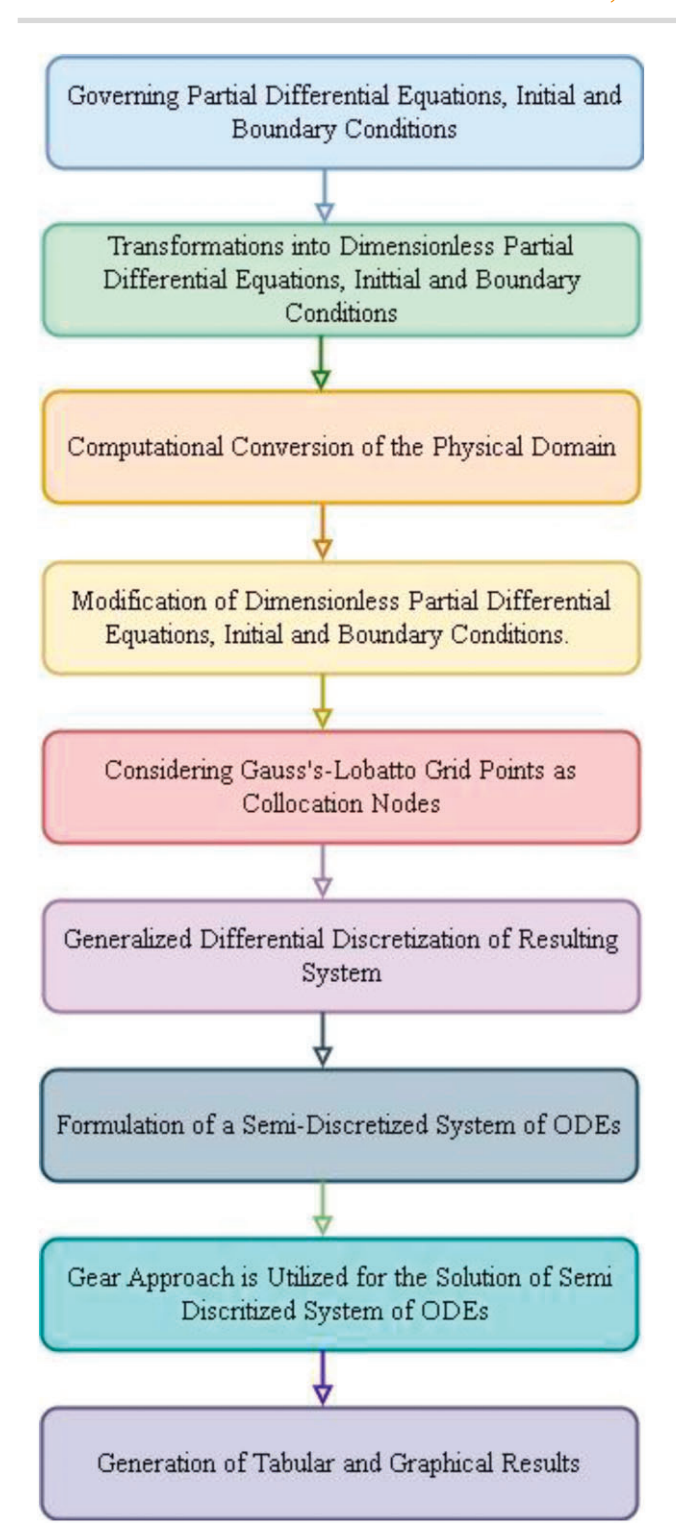


Figure 2: Flowchart: Gear generalized differential quadrature method.

information from several prior steps to calculate the answer at the current time step.

### 2. Mathematical formulation

Consider the unsteady flow of nanofluid  $(TiO_2(s) - C_2H_6O_2(bf))$ over an oscillating stretching surface. The flow is influenced by a constant magnetic field of strength  $B_0$  as shown in Fig. 1. The electric conductivity is assumed to be temperature-dependent (Makinde & Onyejekwe, 2011). The viscous dissipation function

is incorporated in the energy equation to include the effects of frictional heating between the adjacent layers of the nanofluid. The system of Cartesian coordinates is chosen. The  $\bar{X}$  – axis and  $\bar{Y}$  – axis are measured along and normal to the oscillating surface having velocity  $U_{\omega} = \tilde{U}(\bar{X}) \sin(\varpi \bar{t})$ , where  $\tilde{U}(\bar{X}) = U_0 \bar{X}$ . The temperature at  $\bar{Y} = 0$  is denoted by  $T_w$  and assumed to be of the form  $T_w = T_\infty + T_0 \bar{X}^2$ , where  $T_\infty$  indicates the ambient temperature. In these conditions, the leading governing equations are listed below (Qasim et al., 2020; Sheikh & Abbas, 2015; Wakif et al., 2019)

$$\frac{\partial \mathbf{U}}{\partial \bar{\mathbf{X}}} + \frac{\partial \mathbf{V}}{\partial \bar{\mathbf{Y}}} = 0,\tag{1}$$

$$\frac{\partial U}{\partial \bar{t}} + U \frac{\partial U}{\partial \bar{X}} + V \frac{\partial U}{\partial \bar{Y}} = \frac{\mu_{nf}}{\rho_{nf}} \frac{\partial^2 U}{\partial \bar{Y}^2} - \frac{\sigma_{nf} (T) B_o^2}{\rho_{nf}} U, \tag{2}$$

$$\left(\rho C_{p}\right)_{nf}\left(\frac{\partial T}{\partial \bar{t}}+U\frac{\partial T}{\partial \bar{X}}+V\frac{\partial T}{\partial \bar{Y}}\right)=k_{nf}\frac{\partial^{2} T}{\partial \bar{Y}^{2}}+\sigma_{nf}\left(T\right)B_{o}^{2}U^{2}$$

$$+\mu_{nf}\left(\frac{\partial U}{\partial \bar{Y}}\right)^2$$
. (3)

Following are the initial and boundary conditions:

$$\begin{array}{l} U(\overline{X}, \overline{t}) = U_w = \widetilde{U}(\overline{X}) \sin(\varpi \overline{t}) \\ V = 0 \\ T(\overline{X}, \overline{t}) = T_w = T_\infty + T_0 \overline{X}^2 \end{array} \right\} at \overline{Y} = 0 \quad \forall \ \overline{t} > 0,$$
 (5)

$$\left\{ \begin{array}{l}
 U \to 0 \\
 V \to 0 \\
 T \to T_{\infty}
 \end{array} \right\} \quad \text{as } \overline{Y} \to \infty \quad \forall \, \overline{t} > 0. \tag{6}$$

Equation (1) shows the continuity equation for an incompressible fluid in differential form. It demonstrates that no net fluid flows into or out of the control volume, suggesting that mass is preserved. Equation (2) is based on applying Newton's second law of motion to a fluid element. Local acceleration is the first term on the left-hand side, and it displays the temporal rate of change in the velocity component U. The convective acceleration is represented by the second and third terms on the left side of Equation (2). The first term on the right-hand side of Equation (2) shows viscous force, while the last term is body force due to the applied magnetic field. Equation (3) is called the energy equation and is derived using the energy conservation law. The first term (called a transient term) on the left-hand side of the energy equation shows the temperature change rate with time; it is the unsteady or transient part of the energy equation. The second and third term (convective term) represent the convection of energy due to the fluid's bulk motion in the x and y directions. It shows how temperature is transported from one point to another as the fluid flows with U and V components of velocity. The first term on the right-hand side of Equation (3) indicates how heat is conducted within the fluid. It is the form of thermal diffusion rate due to temperature gradients in y direction. The second last term shows the Joule heating, and the last term shows the viscous dissipation.

Here,  $(\mu_{nf}, \rho_{nf}, (C_p)_{nf}, k_{nf})$  are defined in Table 1, whereas  $\sigma_{nf}(T)$ shows the temperature-dependent electric conductivity of the nanofluid as defined below.

$$\sigma_{nf}\left(\mathbf{T}\right) = \sigma_{bf}\left(\mathbf{T}\right) \left[1 + \frac{3\left(\frac{\sigma_{s}}{\sigma_{bf}\left(\mathbf{T}\right)} - 1\right)\varphi}{\frac{\sigma_{s}}{\sigma_{bf}\left(\mathbf{T}\right)} + 2 - \left(\frac{\sigma_{s}}{\sigma_{bf}\left(\mathbf{T}\right)} - 1\right)\varphi}\right].$$
 (7)

Further,  $\sigma_{bf}(T) = (\sigma_{bf})_{\infty}[1 + \Lambda(\frac{T - T_{\infty}}{T_{\omega} - T_{\infty}})]$ , with  $(\sigma_{bf})_{\infty}$  is the thermal conductivity of base fluid beyond the thermal boundary layer.

 Table 3: Physical parameters with symbols, expressions, default values, and selected values.

Parameters	Symbols and expressions	Default values	Range of values	
Nanoparticles' volume fraction	φ	0.02	{0.00, 0.02, 0.04, 0.06}	
Strouhal number	$S(=\frac{\varpi}{U_o})$	0.5	{0.5, 1.0, 1.5, 2.0}	
Eckert number	$Ec \langle = \frac{U_0^2}{C_{bf}T_0} \rangle$	0.04	{0.04, 0.08, 0.12, 0.16}	
Prandtl number	$\Pr \langle = \frac{\nu_{bf} (\rho C_p)_{bf}}{k_{bf}} \rangle$	150.4 583 333 333	Unchanged	
Temperature difference parameter	$\chi \langle = \frac{T_{\infty}}{T_{w} - T_{\infty}} \rangle$	1	{1.0, 1.2, 1.4, 1.6}	
Variable electric conductivity parameter	Λ	3	{0, 1, 2, 3}	
Magnetic parameter	$H_0 \langle = \sqrt{\frac{(\sigma_{bf})_{\infty} B_0^2}{\rho_{bf} U_0}} \rangle$	3	{3, 4, 5, 6}	

Table 4: Comparison with existing literature.

$\left\{\tau = \frac{\pi}{6}, S = 1, Pr = 6, H_0 = 0, \varphi = 0, Ec = 1, \Lambda = 0, N = 100, Y_{\infty} = 5, \Delta\tau = 10^{-5}, \varepsilon = 10^{-10}\right\}$						
	Present results	(Afridi, Ashraf et al., 2022)				
C <sub>fr</sub> 0.82 046 987	Nu <sub>r</sub> 2.18 301 195	C <sub>fr</sub> 0.82 046 987	Nu <sub>r</sub> 2.18 301 195			

Table 5: Convergence C<sub>fr</sub>.

	$\{\tau = \frac{\pi}{6}, S = 0.5, \varphi = 0.02, H_0 = 3, \Lambda = 3, Ec = 0.04, \varepsilon = 10^{-10}\}$									
N	$\Delta \tau =$	≈ 10 <sup>-3</sup>	$\Delta \tau =$	± 10 <sup>−4</sup>	$\Delta \tau = 10^{-5}$					
	$Y_{\infty} = 2.5$	$Y_{\infty} = 5$	$Y_{\infty} = 2.5$	$Y_{\infty} = 5$	$Y_{\infty} = 2.5$	$Y_{\infty} = 5$				
5	0.87 465 598	0.48 498 483	0.87 542 900	0.48 541 044	0.87 556 836	0.48 548 704				
10	1.83 955 591	1.64 880 191	1.84 109 975	1.65 022 818	1.84 138 730	1.65 049 094				
15	2.35 891 384	1.88 334 582	2.36 177 107	1.88 508 197	2.36 223 082	1.88 539 260				
20	2.52 472 377	2.29 299 180	2.52 708 537	2.29 587 033	2.52 749 714	2.29 632 928				
25	2.50 743 614	2.53 676 024	2.50 997 978	2.53 924 585	2.51 041 282	2.53 967 128				
30	2.51 134 104	2.51 085 097	2.51 384 469	2.51 325 799	2.51 427 283	2.51 367 524				
35	2.51 070 121	2.50 685 072	2.51 321 129	2.50 940 123	2.51 364 020	2.50 983 506				
40	2.51 077 147	2.51 200 835	2.51 328 059	2.51 451 616	2.51 370 939	2.51494478				
45	2.51 076 430	2.51 070 737	2.51 327 355	2.51 321 369	2.51 370 236	2.51364216				
50	2.51 076 502	2.51 071 805	2.51 327 425	2.51 322 838	2.51 370 306	2.51 365 732				
60	2.51 076 494	2.51 076 137	2.51 327 417	2.51 327 060	2.51 370 298	2.51 369 942				
70	2.51 076 494	2.51 076 400	2.51 327 417	2.51 327 323	2.51 370 298	2.51370204				
80	2.51 076 494	2.51 076 388	2.51 327 417	2.51 327 311	2.51 370 298	2.51370192				
90	2.51 076 494	2.51 076 389	2.51 327 417	2.51 327 312	2.51 370 298	2.51 370 193				
100	2.51 076 494	2.51 076 389	2.51 327 417	2.51 327 312	2.51 370 298	2.51370193				
110	2.51 076 494	2.51 076 389	2.51 327 417	2.51 327 312	2.51 370 298	2.51370193				
120	2.51 076 494	2.51 076 389	2.51 327 417	2.51 327 312	2.51 370 298	2.51370193				
130	2.51 076 494	2.51 076 389	2.51 327 417	2.51 327 312	2.51 370 298	2.51370193				
140	2.51 076 494	2.51 076 389	2.51 327 417	2.51 327 312	2.51 370 298	2.51370193				
150	2.51 076 494	2.51 076 389	2.51 327 417	2.51 327 312	2.51 370 298	2.51 370 193				

The electric conductivity of base fluid inside the boundary layer is considered constant in most articles in the literature, which is incorrect. Given the prevalence of this mistake in scholarly works, it is essential to address it here. The subscripts bf, s, nf, respectively, represent base fluid, solid nanoparticles, and nanofluid. The values of the thermophysical quantities of ethylene glycol and titanium dioxide are tabulated in Table 2.

Similarity variables are defined as given below.

$$Y = \sqrt{\frac{U_0}{\nu_{bf}}}\overline{Y}, \ \psi = \overline{X}\sqrt{U_0\nu_{bf}}\ U^*\left(Y,\tau\right), \ \tau = \varpi\bar{t}, \ T^* = \frac{T-T_\infty}{T_w-T_\infty}. \ \ (8)$$

The components of velocity  $\boldsymbol{U}$  and  $\boldsymbol{V}$  are defined in terms of stream function as follows:

$$U = \frac{\partial \psi}{\partial \bar{Y}}$$
 and  $V = -\frac{\partial \psi}{\partial \bar{X}}$ . (9)

Using Equation (9), (U, V) can be written as

$$U = \tilde{U}\left(\tilde{X}\right) \frac{\partial U^{*}\left(Y,\tau\right)}{\partial Y} \quad \text{and} \quad V = -\sqrt{U_{o}\nu_{bf}} \ U^{*}\left(Y,\tau\right). \tag{10} \label{eq:10}$$

Employing similarity variables, the dimensional governing equations and boundary conditions take the following form:

**Table 6:** Convergence Nu<sub>r</sub>.

	$\{\tau = \frac{\pi}{6}, S = 0.5, \varphi = 0.02, H_0 = 3, \Lambda = 3, Ec = 0.04, \varepsilon = 10^{-10}\}$									
N	$\Delta \tau =$	10 <sup>-3</sup>	$\Delta \tau =$	10 <sup>-4</sup>	$\Delta \tau = 10^{-5}$					
	$Y_{\infty} = 2.5$	$Y_{\infty} = 5$	$Y_{\infty} = 2.5$	$Y_{\infty} = 5$	$Y_{\infty} = 2.5$	$Y_{\infty} = 5$				
5	5.17 862 382	2.68 597 203	5.17 896 217	2.68 637 449	5.17 905 294	2.68 645 082				
10	11.84 520 416	10.36 880 996	11.83 427 797	10.36 510 455	11.83 301 904	10.36 472 491				
15	10.74031660	11.43 238 933	10.73 544 150	11.42 246 132	10.73 489 904	11.42 133 407				
20	10.72 786 819	10.73 001 906	10.72 201 505	10.72 555 233	10.72 133 452	10.72 506 953				
25	10.71696670	10.71 994 195	10.71 110 335	10.71 421 525	10.71 042 301	10.71 354 955				
30	10.71818392	10.72 750 903	10.71 232 441	10.72 158 368	10.71 164 439	10.72 089 493				
35	10.71809022	10.71 660 622	10.71 223 040	10.71 074 271	10.71 155 036	10.71 006 239				
40	10.71810019	10.71 792 987	10.71 224 035	10.71 207 570	10.71 156 031	10.71 139 633				
45	10.71809931	10.71 819 281	10.71 223 949	10.71 233 155	10.71 155 945	10.71 165 133				
50	10.71 809 936	10.71 808 316	10.71 223 954	10.71 222 350	10.71 155 950	10.71 154 348				
60	10.71809936	10.71 810 024	10.71 223 954	10.71 224 041	10.71 155 950	10.71 156 037				
70	10.71809936	10.71 810 026	10.71 223 954	10.71 224 044	10.71 155 950	10.71 156 040				
80	10.71809936	10.71 810 026	10.71 223 954	10.71 224 043	10.71 155 950	10.71 156 040				
90	10.71809936	10.71 810 026	10.71 223 954	10.71 224 043	10.71 155 950	10.71 156 040				
100	10.71809936	10.71 810 026	10.71 223 954	10.71 224 043	10.71 155 950	10.71 156 040				
110	10.71 809 936	10.71 810 026	10.71 223 954	10.71 224 043	10.71 155 950	10.71 156 040				
120	10.71809936	10.71 810 026	10.71 223 954	10.71 224 043	10.71 155 950	10.71 156 040				
130	10.71 809 936	10.71 810 026	10.71 223 954	10.71 224 043	10.71 155 950	10.71 156 040				
140	10.71809936	10.71 810 026	10.71 223 954	10.71 224 043	10.71 155 950	10.71 156 040				
150	10.71 809 936	10.71 810 026	10.71 223 954	10.71 224 043	10.71 155 950	10.71 156 040				

Table 7: Numerical results.

						G	GDQM's results whe	en $\{N=150, Y_{\infty}=5, \varepsilon=1\}$	$=10^{-10}$ }
τ	S	$oldsymbol{arphi}$	$H_0$	Λ	Ec	$C_{\mathit{fr}}$	Slope	Nu <sub>r</sub>	Slope
$\frac{\pi}{10}$	0.5	0.02	3	3	0.04	1.53 933 179	3.03 944 859	11.48 449 608	- 3.79330625
$\frac{3\pi}{10}$						4.13 359 306		9.29 690 420	
$\frac{2\pi}{5}$ $\frac{\pi}{2}$						4.93 017 672		7.77 658 559	
$\frac{\pi}{2}$						5.23 107 598		6.80 257 592	
π 10	0.5	0.02	3	3	0.04	1.53 933 179	0.06 813 232	11.48 449 608	5.32 866 230
10	1.0					1.54 460 951		14.63 790 639	
	1.5					1.58 555 240		17.23 885 647	
	2.0					1.63 923 803		19.49 861 656	
π 6	0.5	0.00	3	3	0.04	2.30 354 516	15.18 222 720	10.17 607 708	19.10 175 850
0		0.02				2.51 370 193		10.71 156 040	
		0.04				2.79 572 542		11.04 394 191	
		0.06				3.22 168 581		11.33 873 381	
<u>π</u> 6	0.5	0.02	3	3	0.04	2.51 370 193	1.08 720 750	10.71 156 040	- 2.35361705
O			4			3.52 367 980		8.73 012 975	
			5			4.61 943 184		6.35 462 148	
			6			5.77 247 626		3.65 800 631	
<u>π</u>	0.5	0.02	3	0	0.04	1.78 206 294	0.24 388 383	12.19610833	- 0.49485237
0				1		2.02726934		11.70 339 901	
				2		2.27 119 076		11.20 851 906	
				3		2.51 370 193		10.71 156 040	
<u>π</u> 6	0.5	0.02	3	3	0.04	2.51 370 193	1.40 416 372	10.71 156 040	<b>-</b> 69.05412677
0					0.08	2.56 834 042		8.08 704 477	
					0.12	2.62 450 366		5.32 721 258	
					0.16	2.68 220 268		2.42 428 756	

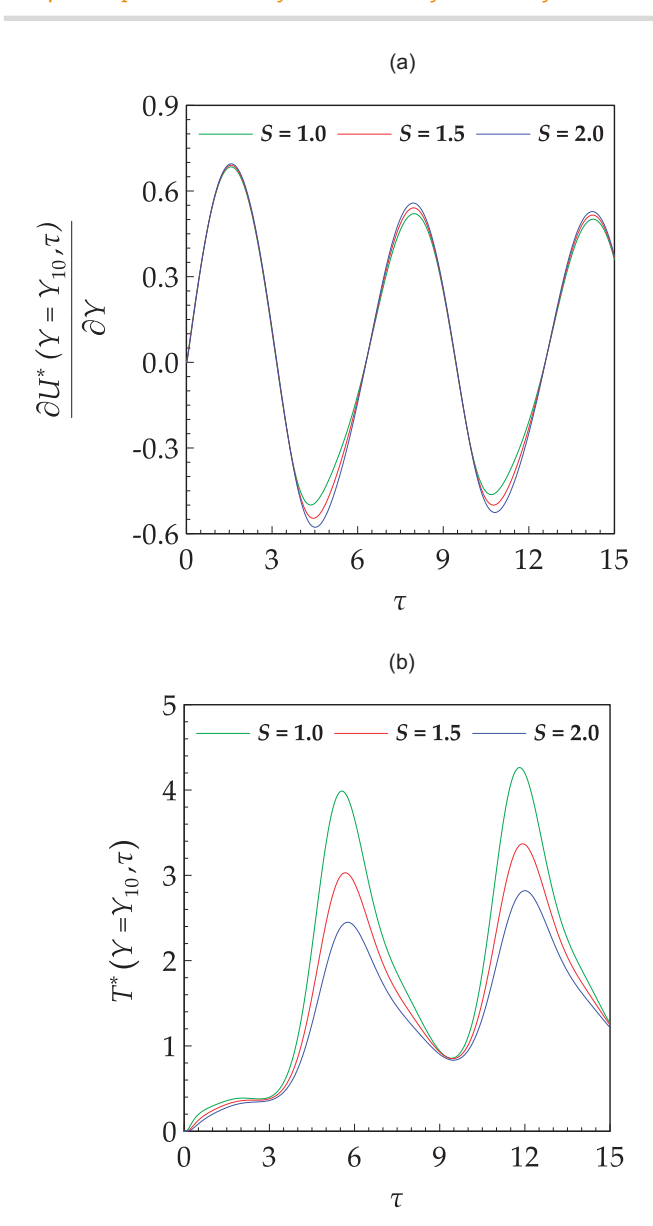


**Figure 3:** Time series profile: Effects of S on (a)  $\frac{\partial U^*}{\partial Y}$  (b)  $T^*$ .

$$\begin{split} \frac{N_1}{N_2} \frac{\partial^3 U^*}{\partial Y^3} + U^* \frac{\partial^2 U^*}{\partial Y^2} - \left(\frac{\partial U^*}{\partial Y}\right)^2 - H_0^2 \frac{N_3}{N_2} \frac{\partial U^*}{\partial Y} = S \frac{\partial^2 U^*}{\partial Y \partial \tau}, \qquad (11) \\ \frac{N_5}{Pr} \frac{\partial^2 T^*}{\partial Y^2} + N_4 \left(U^* \frac{\partial T^*}{\partial Y} - 2T^* \frac{\partial U^*}{\partial Y}\right) \end{split}$$

$$+ \operatorname{Ec}\left(N_1\left(\frac{\partial^2 U^*}{\partial Y^2}\right)^2 + N_3 H_0^2\left(\frac{\partial U^*}{\partial Y}\right)^2\right) = N_4 \operatorname{S} \frac{\partial T^*}{\partial \tau}, \qquad (12)$$

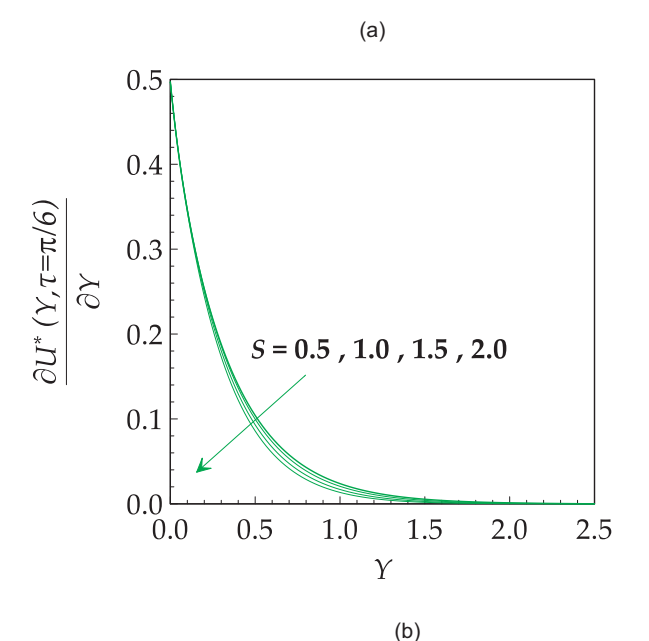
$$\frac{\partial U^*}{\partial Y}(Y, \tau = 0) = 0 
T^*(Y, \tau = 0) = 0$$
(13)

$$\frac{\partial U^*}{\partial Y}(Y, \tau = 0) = 0 \\
T^*(Y, \tau = 0) = 0
\end{aligned}, (13)$$

$$\frac{\partial U^*}{\partial Y}(0, \tau) = \sin(\tau) \\
U^*(0, \tau) = 0 \\
T^*(0, \tau) = 1$$

$$\frac{\partial U^*}{\partial Y} (Y \to \infty, \tau) \to 0 
T^* (Y \to \infty, \tau) \to 0$$

$$\forall \tau > 0.$$
(15)



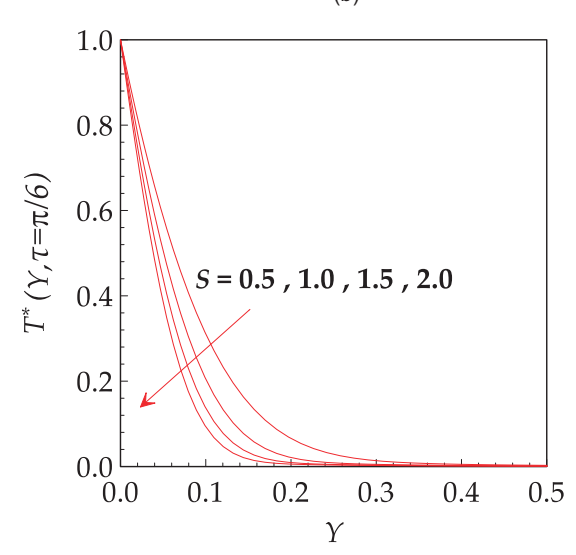


**Figure 4:** Effects of S on (a)  $\frac{\partial U^*}{\partial Y}$  (b)  $T^*$ .

Here,

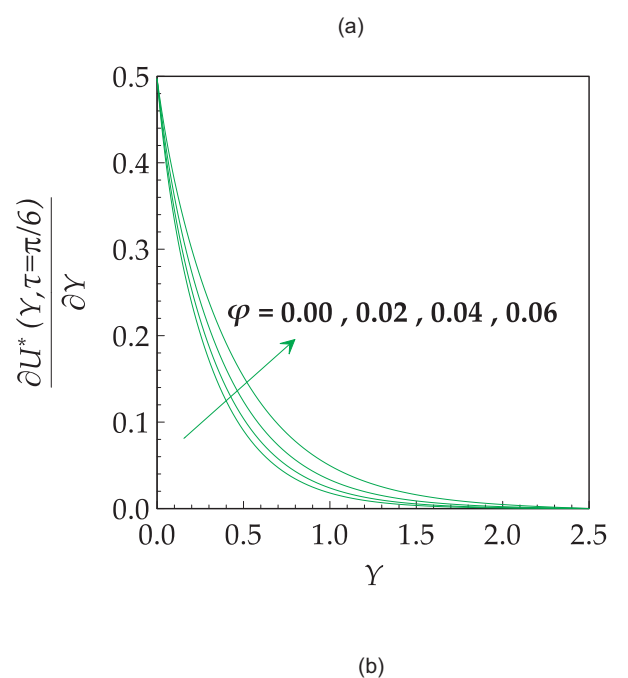
$$\begin{split} N_{1} &= \frac{\mu_{nf}}{\mu_{bf}}, N_{2} \frac{\rho_{nf}}{\rho_{bf}} \\ N_{3} &= \frac{\sigma_{nf}\left(T\right)}{\left(\sigma_{nf}\right)_{\infty}} = \left(1 + \Lambda T^{*}\right) \left[1 + \frac{\left(\frac{3}{\left(1 + \Lambda T^{*}\right)} \frac{\sigma_{s}}{\left(\sigma_{bf}\right)_{\infty}} - 1\right) \varphi}{\frac{1}{\left(1 + \Lambda T^{*}\right)} \frac{\sigma_{s}}{\left(\sigma_{bf}\right)_{\infty}} + 2 - \left(\frac{1}{\left(1 + \Lambda T^{*}\right)} \frac{\sigma_{s}}{\left(\sigma_{bf}\right)_{\infty}} - 1\right) \varphi}\right] \\ N_{4} &= \frac{\left(\rho C_{p}\right)_{nf}}{\left(\rho C_{p}\right)_{nf}}, N_{5} = \frac{k_{nf}}{k_{bf}} \end{split}$$

$$(16)$$

The expressions for local skin friction coefficient  $C_{fx}$  and Nusselt number Nu<sub>x</sub>

$$C_{fr} = -Re_{x}^{1/2}C_{fx} = -N_{1}\frac{\partial^{2}U^{*}}{\partial Y^{2}}(0,\tau),$$

$$Nu_{r} = Re_{x}^{-1/2}Nu = -N_{5}\frac{\partial T^{*}}{\partial Y}(0,\tau).$$
(17)



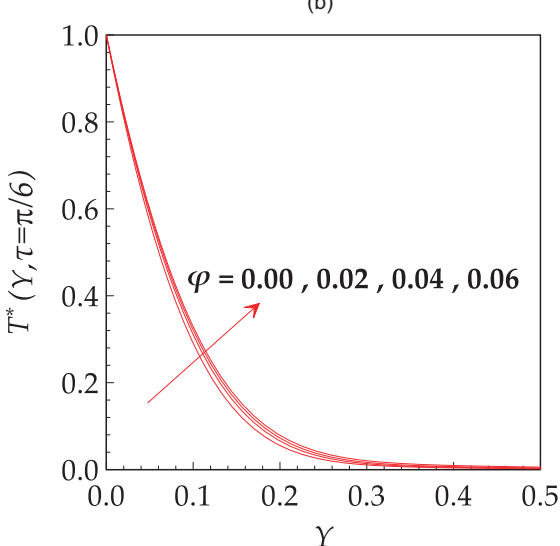


**Figure 5:** Effects of  $\varphi$  on (a)  $\frac{\partial U^*}{\partial Y}$  (b)  $T^*$ .

# 3. Minimization of entropy generation

Considering the variable electric conductivity, the rate of entropy generation  $(\dot{E}_{\mathit{qen}}^{\prime\prime\prime})$  in a dissipative nanofluid flow can be formulated as

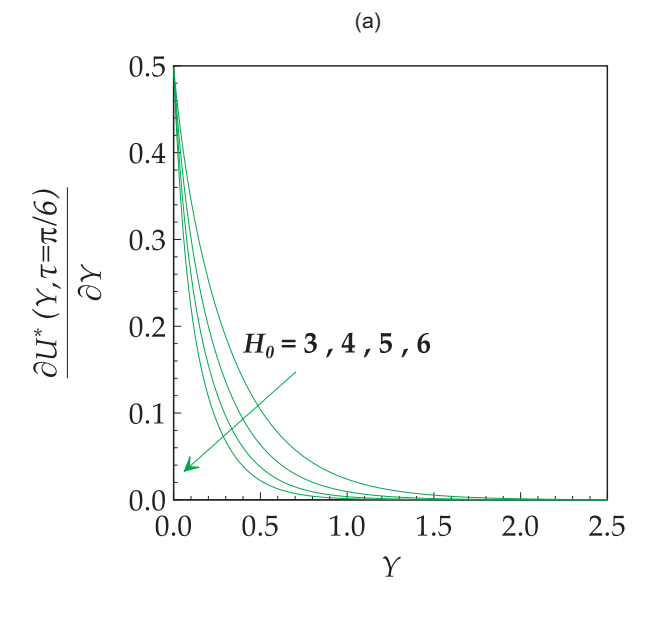
$$\left(\dot{\mathbf{E}}_{gen}^{""}\right) = \frac{k_{nf}}{T^2} \left(\frac{\partial \mathbf{T}}{\partial \bar{\mathbf{Y}}}\right)^2 + \frac{\sigma_{nf}(\mathbf{T}) \,\mathbf{B}_0^2 \mathbf{U}^2}{\mathbf{T}} + \frac{\mu_{nf}}{\mathbf{T}} \left(\frac{\partial \mathbf{U}}{\partial \bar{\mathbf{Y}}}\right)^2. \tag{18}$$

Using Equation (8), Equation (18) takes the following form

$$Ns = \frac{\dot{E}_{gen}^{"}}{\left(\dot{E}_{gen}^{"}\right)_o} = \frac{N_5}{(T^* + \chi)^2} \left(\frac{\partial T^*}{\partial Y}\right)^2 + N_3 \frac{H_0^2 Ec \, Pr}{(T^* + \chi)} \left(\frac{\partial U^*}{\partial Y}\right)^2 + N_1 \, Pr \, \frac{Ec}{(T^* + \chi)} \left(\frac{\partial^2 U^*}{\partial^2 y}\right)^2.$$

$$(19)$$

Here, Ns and  $(\dot{E}_{qen}^{'''})_{o}$ , respectively, indicate dimensionless and characteristic entropy. A parameter of irreversibility is introduced to assess the relative magnitude of entropy generation due to heat transfer compared to the total entropy generation. This parame-



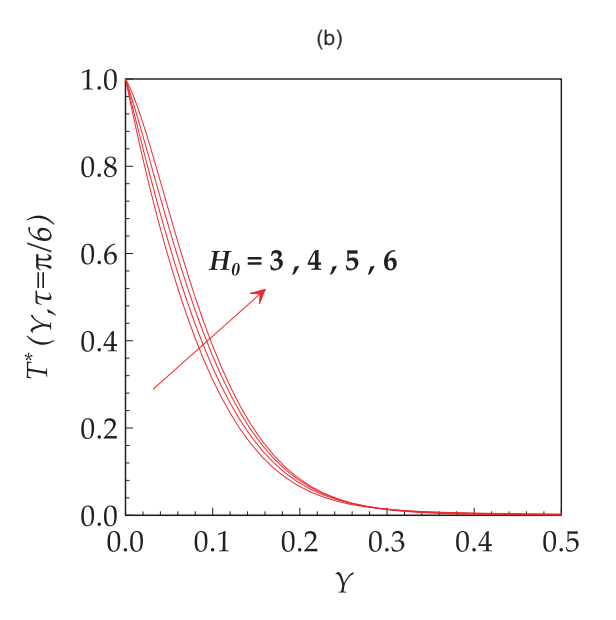


Figure 6: Effects of  $H_0$  on (a)  $\frac{\partial U^*}{\partial V}$  (b)  $T^*$ .

ter termed the Bejan number is precisely defined as

$$Be = \frac{\frac{k_{nf}}{T^{2}} \left(\frac{\partial T}{\partial Y}\right)^{2}}{\frac{k_{nf}}{T^{2}} \left(\frac{\partial T}{\partial Y}\right)^{2} + \frac{\sigma_{nf}(T)B_{0}^{2}U^{2}}{T} + \frac{\mu_{nf}}{T} \left(\frac{\partial U}{\partial Y}\right)^{2}}.$$
 (20)

Equation (20) takes the following form after the utilization of Equation (8):

$$Be = \frac{N_5 \left(\frac{\partial T^*}{\partial Y}\right)^2}{N_5 \left(\frac{\partial T^*}{\partial Y}\right)^2 + \Pr Ec \left(T^* + \chi\right) \left(N_1 \left(\frac{\partial^2 U^*}{\partial^2 U}\right)^2 + N_3 H_0^2 \left(\frac{\partial U^*}{\partial Y}\right)^2\right)}. \quad (21)$$

## 4. Results and discussion

The numerical solution of nonlinear PDEs represented by Equations (11) and (12) is successfully obtained using the GGDQM. The key steps of GGDQM are depicted in the Figure 2. In the entire process of simulations, the default and selected values

2.5

0.5

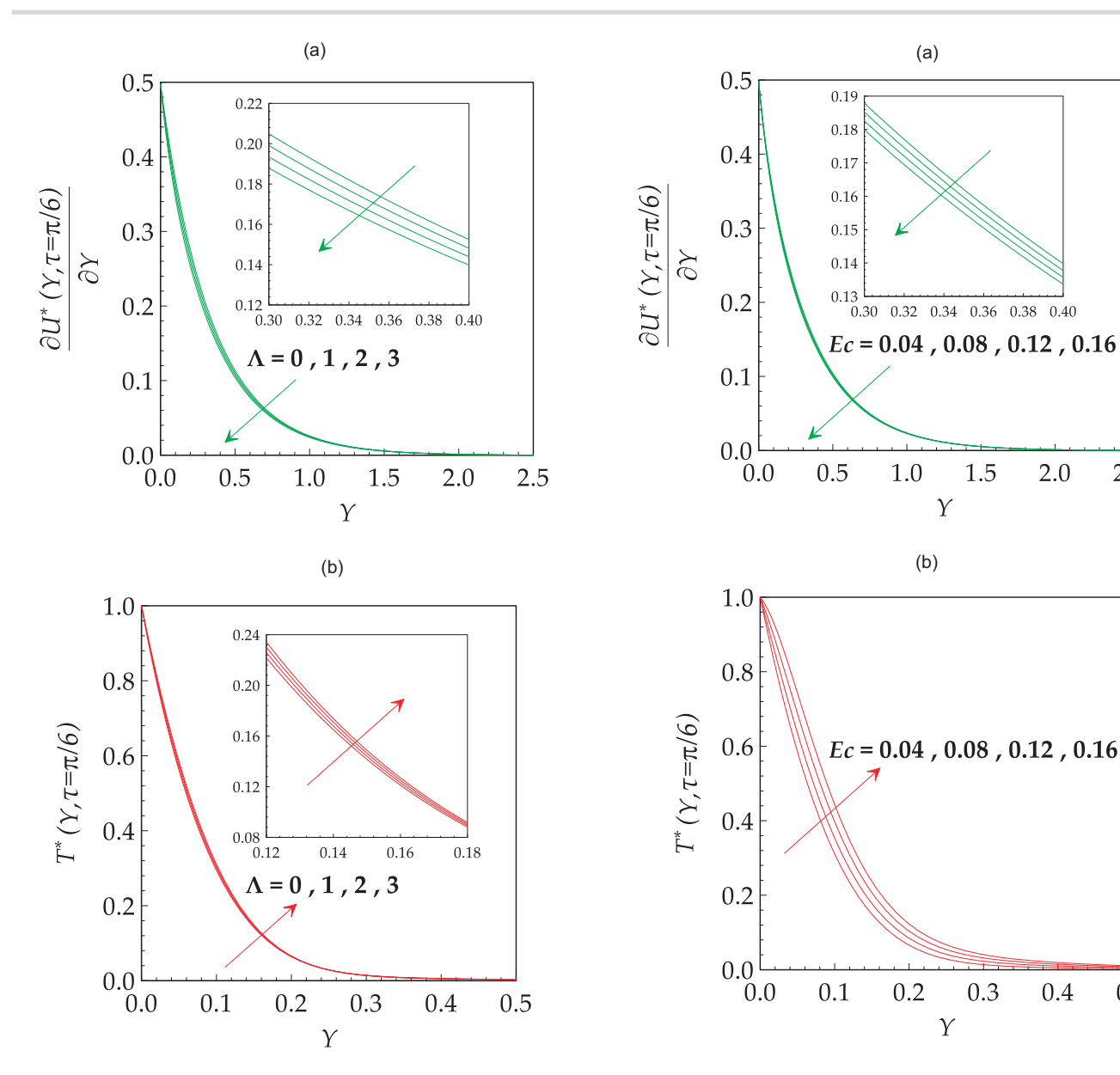


**Figure 7:** Effects of  $\Lambda$  on (a)  $\frac{\partial U^*}{\partial Y}$  (b)  $T^*$ .

of parameters are explicitly shown in Table 3. To validate the accuracy of the current numerical technique, the outcomes for  $Nu_r$  and  $C_{fr}$  were compared with the findings reported by (Afridi, Ashraf et al., 2022), as presented in Table 4. The spatial domain  $Y \in [0,~\infty)$  is truncated to the  $Y \in [0,~Y_{\infty} = 5].$  The justification for the selection of a semi-infinite domain is seen in Tables 5 and 6. We used the time step size  $\Delta \tau = 10^{-5}$  and the number of mesh points N = 90. These numbers were considered satisfactory for producing accurate and consistent results because increased Gauss-Lobbato grid points did not result in different numerical results. The results indicate a significant level of agreement between the two data sets, thereby supporting the validity of the present numerical method. Tables 5 and 6 respectively exhibit the relationship between the convergence of  $Nu_r$  and  $C_{fr}$  to N(number of grid points)  $Y_{\infty}$  and  $\Delta\tau$  (time step). Upon careful examination of the data shown in Tables 5 and 6, it becomes evident that the order of accuracy experiences an upward trend as the temporal time step  $\Delta au$  decreases. This trend indicates that smaller time steps contribute to higher accuracy levels in

**Figure 8:** Effects of Ec on (a)  $\frac{\partial U^*}{\partial Y}$  (b) T\*.

numerical calculations. The analysis of the numerical results highlights that ensuring convergence for GGDQM can be achieved by utilizing a limited number of mesh points. Table 7 illustrates the behavior of  $Nu_r$  and  $C_{fr}$  under different variations of emerging parameters. Moreover, applying the slope linear regression method aids in estimating the rate of change in shear stresses and heat transfer at the sheet. The analysis indicates that the  $C_{fr}$  exhibits a rise with the Eckert number, dimensionless time, Strouhal number, nanoparticle volume fraction, magnetic and variable electric conductivity parameters. It is evident from the positive and negative signs of the slope that  $Nu_r$  rises with the Strouhal number and nanoparticle volume fraction but decreases with the magnetic parameter, dimensionless time, Eckert number, and variable electric conductivity parameter.

Figures 3–15 provide detailed visual representations illustrating the relationships between various flow parameters and their corresponding impacts on critical variables such as velocity  $(\frac{\partial U}{\partial Y}(Y,\tau))$ , thermal characteristics  $T(Y,\tau)$ , entropy distribution  $Ns(Y,\tau)$ , and Bejan numbers  $Be(Y,\tau)$ . Figures 3(a) and (b), respectively, illustrate

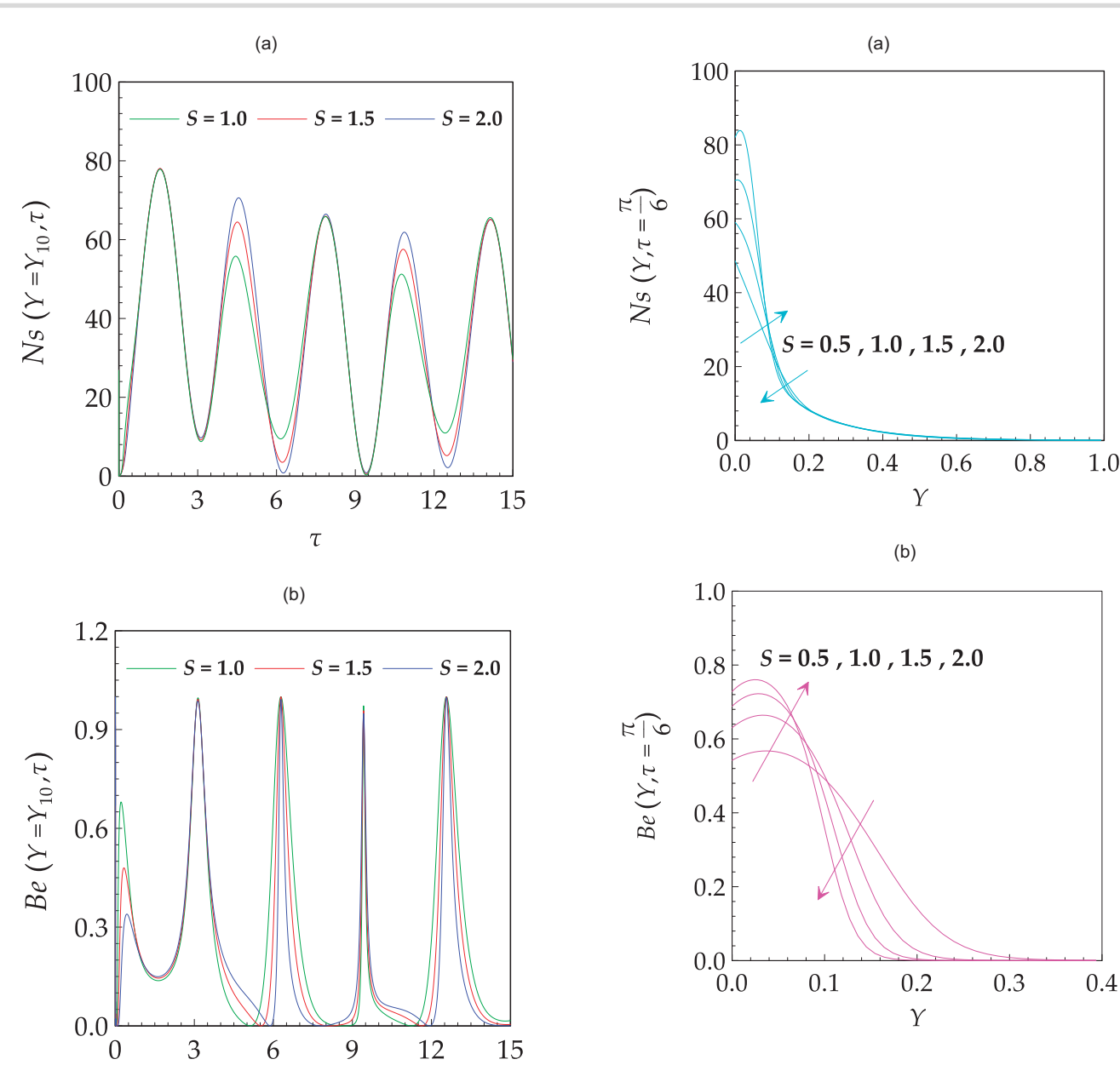


Figure 9: Time series profile: Effects of S on (a) Ns (b) Be.

how the Strouhal number affects the time series of the velocity profile and temperature distribution. Figure 3(a) demonstrates a phase shifting and an increase in the amplitude of the fluid motion by increasing the Strouhal number. Figure 3(b) reflects a decline in temperature profile when the Strouhal number increases. Figure 4(a) describes the impact of the Strouhal number on the velocity profile. The plot reveals a notable trend where an increment in the Strouhal number decelerates the fluid's motion. This phenomenon indicates an inverse relationship between the Strouhal number and velocity profile. Furthermore, Fig. 4(b) findings suggest that as the Strouhal number S increases, the heat transfer from the oscillating surface diminishes correspondingly. This decrease in heat transfer subsequently leads to a lower thermal boundary layer. Figure 5(a) and (b), respectively, depict the influence of varying volume fractions on the velocity and temperature distributions within the boundary layer. A positive correlation be-

τ

Figure 10: Effects of S on (a) Ns (b) Be.

tween the velocity profile and  $\varphi$  in the boundary layer is found, indicating that as  $\varphi$  increases, the velocity profile increases accordingly. Increasing nanoparticle volume fraction improves energy transportation within the fluid, subsequently accelerating the fluid motion. Figure 5(b) demonstrates that the temperature profile expands proportionally with the increase in the value of  $\varphi$ . Higher volume fractions result in elevated thermal conductivity, consequently leading to an augmentation in boundary layer thickness and a subsequent escalation in the temperature profile.

Figures 6(a) and (b), respectively, explain the impact of magnetic parameters on velocity and temperature profiles. Increasing the strength of the magnetic field leads to more vital Lorentz forces, which act to oppose the flow motion. Consequently, the velocity decreases due to increased resistance from the magnetic field, as shown in Fig. 6(a). Figure 6(b) portrays the correlation between the temperature increase and the magnetic field enhancement. This phenomenon occurs due to the increasing Lorentz force, which decelerates the fluid flow, converting kinetic energy into thermal energy. This conversion thereby contributes

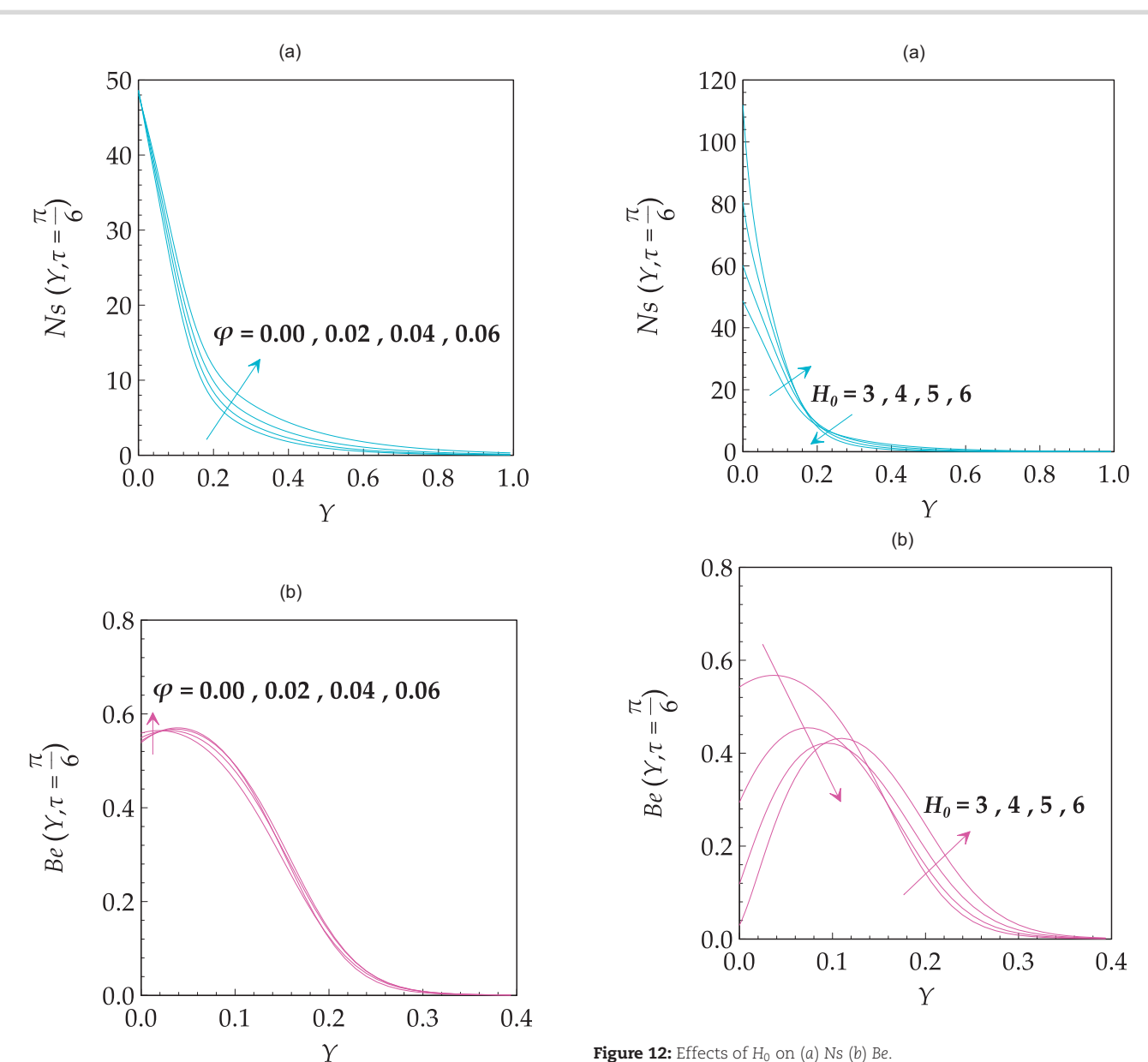


**Figure 11:** Effects of  $\varphi$  on (a) Ns (b) Be.

to the overall elevation in the temperature distribution. Figure 7(a) shows that the velocity profiles decline as the variable electric conductivity parameter increases. Viewed from a physical standpoint, higher variable electric conductivity parameter values result in a more vital magnetic force within the flow, opposing the fluid's motion and dampening the flow's velocity. The damping effect intensifies as conductivity increases, causing the flow velocity to decrease. It is evident from Fig. 7(b) that as the variable electrical conductivity parameter  $\Lambda$  increases, the temperature profile exhibits an enhancement.

As the Eckert number increases, Fig. 8 (a) illustrates that the fluid velocity decreases. It has been noted from Fig. 8(b) that an elevation in Ec values is linked to an increase in the temperature profile. Viewed from a physical standpoint, a surge in Ec values heightens the frictional forces between the fluid layers. This, thus, brings forth the shift of kinetic energy into thermal energy; as a result, there is a noticeable rise in the temperature profile. Con-

Figure 12: Effects of H<sub>0</sub> on (a) Ns (b) Be.

sequently, it can be inferred that variations in Ec values play a crucial role in influencing the thermal dynamics of the system. Figures 9(a) and (b), respectively, reflect how the Strouhal number affects the time series of the entropy generation distribution and the Bejan number. Figure 9(a) demonstrates a phase shift occurring and an increase in the amplitude of the entropy generation by increasing the Strouhal number. Figure 9(b) reflects a decrease in the amplitude of the Bejan number with rising values of the Strouhal number. It is noted from the analysis of Figs. 10(a) and (b) that as the Strouhal number values increase, there is a corresponding rise in entropy and Bejan number in the region at and close to the oscillating boundary, followed by a decline as the distance from the boundary extends beyond a certain point. The entropy generation exhibits a decreasing behavior for growing values of  $\varphi$ , as portrayed in Fig. 11(a). Conversely, the Bejan number shows a reduction with the escalation of parameter  $\varphi$ , except at and close to the stretched oscillating boundary. Entropy augmentation occurs at the surface and its surrounding area as a consequence of the reinforcement of the magnetic field, as portrayed

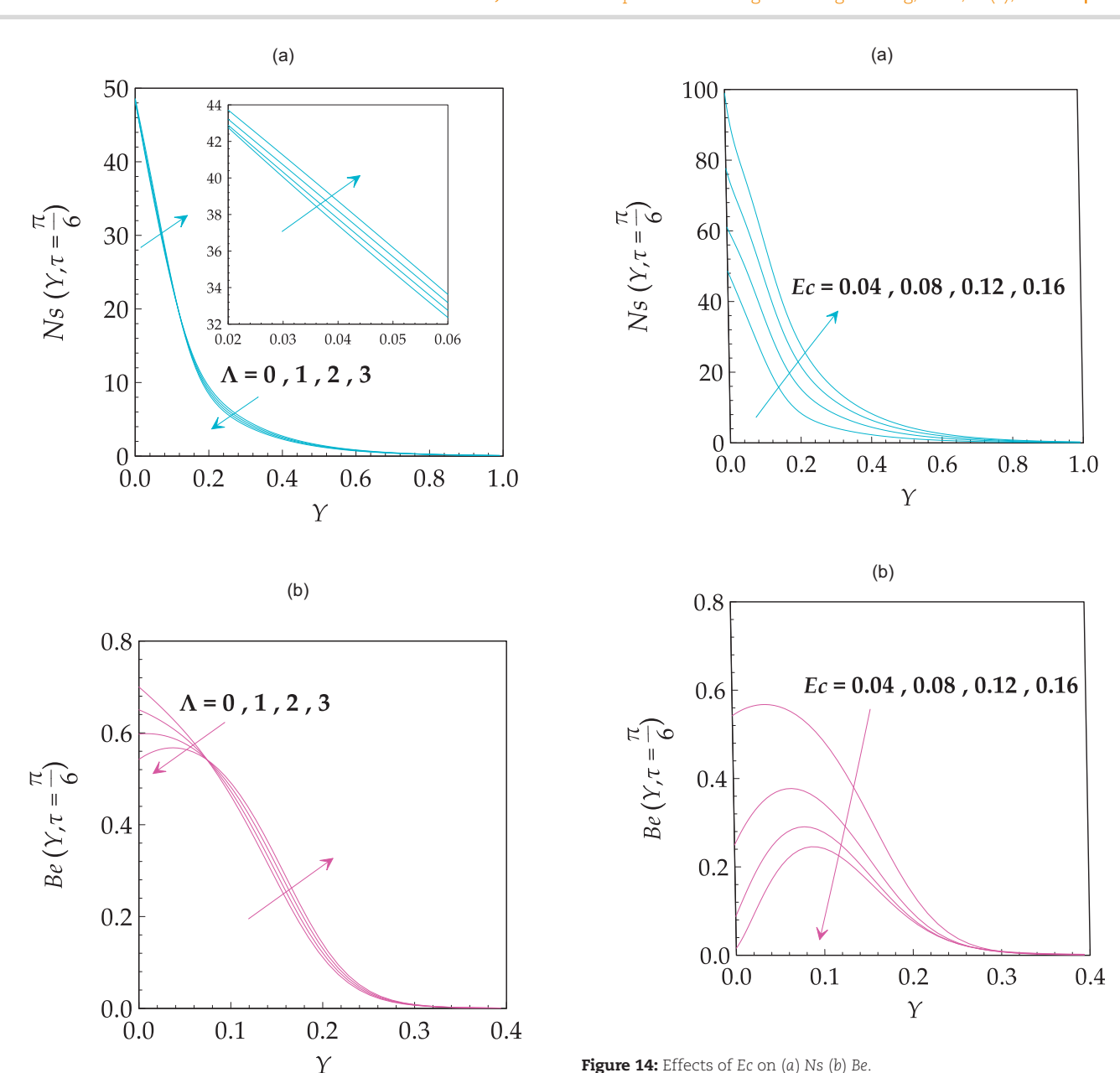
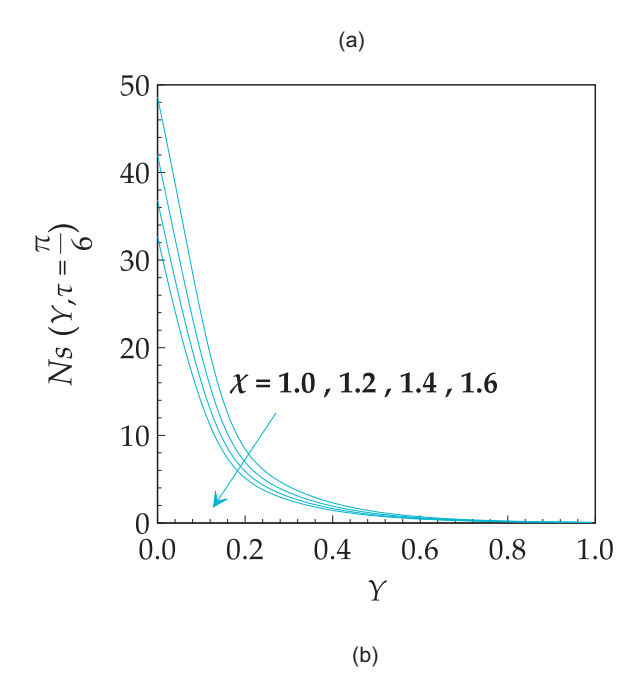


Figure 13: Effects of  $\Lambda$  on (a) Ns (b) Be.

in Fig. 12 (a). An inverse trend is observed in the behavior of the Bejan number with increasing magnetic parameter, as shown in Fig. 12(b).

Figures 13 (a) and (b) depict the impact of variable electric conductivity parameter  $\Lambda$  on Ns and the Bejan number, respectively. With an increase in parameter  $\Lambda$ , the Ns experiences a rise at and near the boundary, but a decrement is observed after a certain vertical distance from the boundary. As  $\Lambda$  escalates, the Bejan number also sees a corresponding increase after a certain vertical distance. Moreover, the decreasing effects were observed near the boundary surface. Heat transfer irreversibility prevails over frictional heating irreversibility at the boundary. Figures 14(a) and (b) depict the changes in entropy generation and Bejan number as the Eckert number increases. It can be noted that there is a noticeable increase in entropy generation as the values of Ec escalate. This phenomenon occurs because of viscous dissipation, which is a process that leads to irreversibility and consequently causes a higher level of entropy generation. Additionally, the graph in Fig. 14(b) reveals a diminishing trend in the Bejan number as the magnitude of the Ec number rises. Figure 15(a) and (b) illustrate how the temperature difference parameters affect entropy generation and Bejan number. A reciprocal relationship is noted between the Ns profile and the temperature difference parameter: as  $\chi$  increases, the entropy profile decreases. Viewed from a physical standpoint, a rise in the temperature difference parameter corresponds to a decline in the operating temperature, leading to a decrease in the heat transfer rate. Therefore, this reduction in heat transfer rate results in a decrease in entropy generation. Alternatively, to minimize entropy generation, which aligns with the primary objective of second law analysis, reducing the  $\chi$  can be pursued. Figure 15(b) exhibits the Bejan number profile for various values of  $\chi$ . Increasing  $\chi$  signifies a diminished temperature difference between the stretching boundary and the ambient fluid. Consequently, thermal irreversibility diminishes, as Fig. 15(b) depicts.

Figure 14: Effects of Ec on (a) Ns (b) Be.



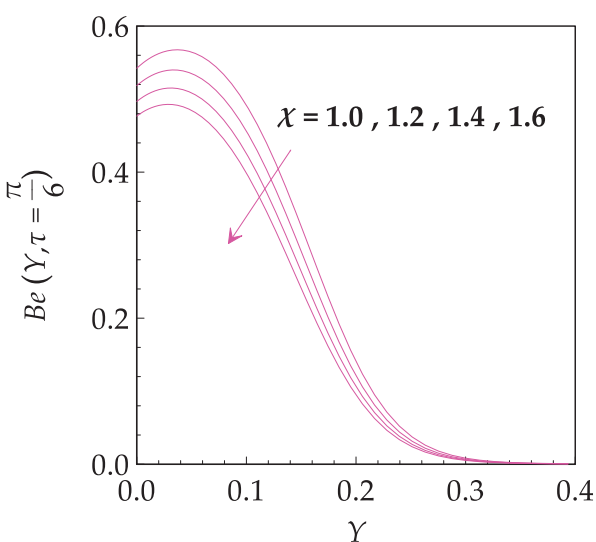


Figure 15: Effects of  $\chi$  on (a) Ns (b) Be.

## 5. Concluding remarks

The ongoing investigation aims to examine heat transfer and entropy generation within a nanofluid flow along an oscillating surface, focusing on viscous dissipation, magnetic field impact, and temperature-dependent electric conductivity. The Corcione model has been adopted to characterize the nanofluid's thermal conductivity and effective viscosity under study. The generalized differential quadrature method (GGDQM) is applied in this study to conduct numerical simulations. The subsequent results outline the most notable findings of our research.

- The self-similar solution to the current problem is only possible in non-isothermal boundary conditions.
- With increase in S there is a decrease in heat transfer, reducing the thermal boundary layer.

- Decrement in heat transfer with increasing parameter S leads to a lower in the thermal boundary layer.
- A positive correlation is found between the velocity profile and  $\varphi$ .
- · Velocity profiles decline as the variable electric conductivity parameter increases. An inverse trend is observed for the temperature profile.
- Skin friction coefficient increases with the Eckert number (Ec), dimensionless time  $(\tau)$ , Strouhal number (S), nanoparticle volume fraction  $(\varphi)$ , magnetic parameter  $(H_0)$ , and variable thermal conductivity parameter ( $\Lambda$ ).
- · Nusselt's number rises with the Strouhal number and nanoparticle volume fraction. However, it decreases with the magnetic parameter, dimensionless time, Eckert number, and variable electric conductivity parameter.
- Both temperature and entropy are enhanced with increasing viscous dissipation parameter (Ec).
- Bejan number shows a reduction with the escalation of parameters  $\varphi$  and Ec.
- With an increase in parameter  $\Lambda$ , Ns experiences a rise at and near the oscillating surface.
- An inverse relationship is observed between Ns and the temperature difference parameter  $(\chi)$ .
- Thermal irreversibly reduces with increasing the parameter

#### **Future works**

The mathematical model shows local non-similarity in the case of constant wall temperature, a topic for further research. However, numerous authors commonly regard local non-similarity as self-similar, treating it as self-similar, which results in inaccurate conclusions. Furthermore, there may be much interest in studying thermal conductivity as a function of temperature, which calls for more research.

## **Conflict of interest statement**

The authors declare that they have no known competing financial interests or personal relationships that could have appeared to influence the work reported in this paper.

### **Author contributions**

Muhammad Idrees Afridi (Investigation, Methodology, Visualization, Writing-original draft, Writing-review & editing), Muhammad Sabaoon Khan (Data curation, Project administration, Validation, Visualization, Writing-original draft, Writing-review & editing), Muhammad Qasim (Conceptualization, Investigation, Methodology, Supervision, Writing—review & editing), and Ali J. Chamkha (Formal analysis, Writing-original draft, Resources, Writing—review & editing, validation)

## Acknowledgments

The first author would like to express his sincere gratitude to Hanjiang Normal University for its generous support and resources, which significantly contributed to the completion of this research.

## Data availability

Data sets generated during the current study are available from the corresponding author on reasonable request.

## References

- Abbas, Z., Wang, Y., Hayat, T., & Oberlack, M. (2009). Slip effects and heat transfer analysis in a viscous fluid over an oscillatory stretching surface. International Journal for Numerical Methods in Fluids, 59, 443-458. https://doi.org/10.1002/fld.1825.
- Adeosun, A. T., & Ukaegbu, J. C. (2022). Effect of the variable electrical conductivity on the thermal stability of the MHD reactive squeezed fluid flow through a channel by a spectral collocation approach. Partial Differential Equations in Applied Mathematics, 5, 100256. https://doi.org/10.1016/j.padiff.2021.100256.
- Adesanya, S. O., Banjo, P. O., & Lebelo, R. S. (2023). Exergy analysis for combustible third-grade fluid flow through a medium with variable electrical conductivity and porous permeability. Mathematics, 11, 1882. https://doi.org/10.3390/math11081882.
- Afridi, M. I., Ashraf, M. U., Qasim, M., & Wakif, A. (2022). Numerical simulation of entropy transport in the oscillating fluid flow with transpiration and internal fluid heating by GGDQM. Waves in Random and Complex Media, **32**, 1–19. https://doi.org/10.1080/17455030 .2022.2067371.
- Afridi, M. I., Chen, Z., & Qasim, M. (2022). Numerical Chebyshev finite difference examination of Lorentz force effect on a dissipative flow with variable thermal conductivity and magnetic heating: Entropy generation minimization. ZAMM—Journal of Applied Mathematics and Mechanics /Zeitschrift Für Angewandte Mathematik Und Mechanik, 102, e202200010. https://doi.org/10.1002/zamm.2 02200010.
- Afridi, M. I., Chen, Z.-M., Qasim, M., & Makinde, O. D. (2024). Computational analysis of entropy generation minimization and heat transfer enhancement in magnetohydrodynamic oscillatory flow of ferrofluids. Journal of Magnetism and Magnetic Materials, 594, 171848. https://doi.org/10.1016/j.jmmm.2024.171848.
- Alharbi, A. A. (2024). Thermal analysis of heat transport in a slip flow of ternary hybrid nanofluid with suction upon a stretching/shrinking sheet. Case Studies in Thermal Engineering, 54, 103965. https://doi.org/10.1016/j.csite.2023.103965.
- Ali, N., Ullah Khan, S., Sajid, M., & Abbas, Z. (2016). MHD flow and heat transfer of couple stress fluid over an oscillatory stretching sheet with heat source/sink in porous medium. Alexandria Engineering Journal, 55, 915-924. https://doi.org/10.1016/j.aej.2016.02.018.
- Alsabery, A. I., Yazdi, M. H., Solomin, E., Öztop, H. F., & Hashim, I. (2022). Evaluation of convection flow and entropy generation in a wavy cubical container with nanofluid and embedded cylinder. Journal of Computational Design and Engineering, 9, 598-615. https: //doi.org/10.1093/jcde/qwac005.
- Ashraf, M. U., Qasim, M., Wakif, A., Afridi, M. I., & Animasaun, I. L. (2020). A generalized differential quadrature algorithm for simulating magnetohydrodynamic peristaltic flow of blood-based nanofluid containing magnetite nanoparticles: A physiological application. Numerical Methods for Partial Differential Equations, 38, 666-692. https://doi.org/10.1002/num.22676.
- Bejan, A. (1979). A study of entropy generation in fundamental convective heat transfer. Journal of Heat Transfer, 101, 718-725. https: //doi.org/10.1115/1.3451063.
- Bejan, A., & Kestin, J. (1983). Entropy Generation through Heat and Fluid Flow. Wiley.
- Bhanvase, B., & Barai, D. (2021). Nanofluids for Heat and Mass Transfer.
- Choi, S. U. S. (1995). Enhancing conductivity of fluids with nanoparticles, ASME Fluid Eng. Division, 231, 99-105.
- Corcione, M. (2011). Empirical correlating equations for predicting the effective thermal conductivity and dynamic viscosity of

- nanofluids. Energy Conversion and Management, 52, 789–793. https: //doi.org/10.1016/j.enconman.2010.06.072.
- Cui, J., Azam, F., Faroog, U., & Hussain, M. (2023). Non-similar thermal transport analysis in entropy optimized magnetic nanofluids flow by considering effective prandtl number model with melting heat transfer and joule heating. Journal of Magnetism and Magnetic Materials, 567, 170331. https://doi.org/10.1016/j.jmmm.2022.1703
- Cui, J., Jan, A., Farooq, U., Hussain, M., & Khan, W. A. (2022). Thermal analysis of radiative Darcy–Forchheimer nanofluid flow across an inclined stretching surface. Nanomaterials, 12, 4291. https://doi.or g/10.3390/nano12234291.
- Faroog, U., Jadoon, A., Hussain, M., & Sheremet, M. (2024). Nonsimilar heat transfer analysis of magnetized flow of Ag-Mgo/water hybrid nanofluid flow through darcy porous medium. ZAMM—Journal of Applied Mathematics and Mechanics /Zeitschrift Für Angewandte Mathematik Und Mechanik, 104, e202200628. https: //doi.org/10.1002/zamm.202200628.
- Ghasemi, S. E., & Hatami, M. (2021). Solar radiation effects on MHD stagnation point flow and heat transfer of a nanofluid over a stretching sheet. Case Studies in Thermal Engineering, 25, 100898. https://doi.org/10.1016/j.csite.2021.100898.
- Gholinia, M., Gholinia, S., Hosseinzadeh, K., & Ganji, D. D. (2018). Investigation on ethylene glycol Nano fluid flow over a vertical permeable circular cylinder under effect of magnetic field. Results in Physics, **9**, 1525–1533. https://doi.org/10.1016/j.rinp.2018.04.070.
- Hatami, M., & Jing, D. (2020). Nanofluids: Mathematical, Numerical, and Experimental Analysis. Academic Press.
- Hussain, S., Hag, F., Ghazwani, H. A., Saleem, M., & Hussain, A. (2024). Entropy optimization in bio-convective chemically reactive flow of micropolar nanomaterial with activation energy and gyrotactic microorganisms. Case Studies in Thermal Engineering, 55, 104131. https://doi.org/10.1016/j.csite.2024.104131.
- Idrees Afridi, M., Chen, Z.-M., & Qasim, M. (2023). Entropy generation in local non-similar dissipative MHD flow of CH3OH + Fe3O4 and C12H26-C15H32 + Fe3O4 ferrofluids. Journal of Magnetism and Magnetic Materials, 586, 171177. https://doi.org/10.1016/j.jmmm.2 023.171177.
- Jena, S., & Mishra, M. K. (2023). Entropy analysis of Cu-Al2O3 based hybrid and Cu based mono nanofluid flows through porous medium: A comparative study. Case Studies in Thermal Engineering, 50, 103463. https://doi.org/10.1016/j.csite.2023.103463.
- Khan, Z. H., Khan, W. A., Tang, J., & Sheremet, M. A. (2020). Entropy generation analysis of triple diffusive flow past a horizontal plate in porous medium. Chemical Engineering Science, 228, 115980. https: //doi.org/10.1016/j.ces.2020.115980.
- Khan, Z. H., Makinde, O. D., Ahmad, R., & Khan, W. A. (2018). Numerical study of unsteady MHD flow and entropy generation in a rotating permeable channel with slip and hall effects. Communications in Theoretical Physics, 70, 641. https://doi.org/10.1088/0253-6 102/70/5/641.
- Makinde, O. D., & Onyejekwe, O. O. (2011). A numerical study of MHD generalized couette flow and heat transfer with variable viscosity and electrical conductivity. Journal of Magnetism and Magnetic Materials, 323, 2757-2763. https://doi.org/10.1016/j.jmmm.2011.05.0
- Minkowycz, W. J., Sparrow, E. M., & Abraham, J. P. (2012). Nanoparticle Heat Transfer and Fluid Flow (Vol. 4). CRC press.
- Mkhatshwa, M. P., Motsa, S. S., & Sibanda, P. (2021). MHD mixed convective radiative flow of Eyring-Powell fluid over an oscillatory stretching sheet using bivariate spectral method on overlapping grids. Heat Transfer, 50, 655-687. https://doi.org/10.1002/htj.21898.

- Nayak, M. K., Wakif, A., Animasaun, I. L., & Alaoui, M. S. H. (2020). Numerical differential quadrature examination of steady mixed convection nanofluid flows over an isothermal thin needle conveying metallic and metallic oxide nanomaterials: A comparative investigation. Arabian Journal for Science and Engineering, 45, 5331-5346. https://doi.org/10.1007/s13369-020-04420-x.
- Noreen, S., & Ain, Q. U. l. (2019). Entropy generation analysis on electroosmotic flow in non-Darcy porous medium via peristaltic pumping. Journal of Thermal Analysis and Calorimetry, 137, 1991-2006. https://doi.org/10.1007/s10973-019-08111-0.
- Noreen, S., Rashidi, M. M., & Qasim, M. (2017). Blood flow analysis with considering nanofluid effects in vertical channel. Applied Nanoscience, 7, 193-199. https://doi.org/10.1007/s13204-0 17-0564-0.
- Qasim, M., Afridi, M. I., Wakif, A., & Saleem, S. (2019). Influence of variable transport properties on nonlinear radioactive jeffrey fluid flow over a disk: Utilization of generalized differential quadrature method. Arabian Journal for Science and Engineering, 44, 5987–5996. https://doi.org/10.1007/s13369-019-03804-y.
- Qasim, M., Ali, Z., Farooq, U., & Lu, D. (2020). Investigation of entropy in two-dimensional peristaltic flow with temperature dependent viscosity, thermal and electrical conductivity. Entropy, 22, 200. https://doi.org/10.3390/e22020200.
- Qasim, M., Ali, Z., Wakif, A., & Boulahia, Z. (2019). Numerical simulation of MHD peristaltic flow with variable electrical conductivity and joule dissipation using generalized differential quadrature method. Communications in Theoretical Physics, 71, 509. https: //doi.org/10.1088/0253-6102/71/5/509.
- Qasim, M., Hayat Khan, Z., Khan, I., & Al-Mdallal, Q. (2017). Analysis of entropy generation in flow of methanol-based nanofluid in a sinusoidal wavy channel. Entropy, 19, 490. https://doi.org/10.339 0/e19100490.
- Rafique, K., Mahmood, Z., Adnan Khan, U., Muhammad, T., El-Rahman, M. A., Bajri, S. A., & El-Wahed Khalifa, H. A. (2024). Numerical investigation of entropy generation of joule heating in non-axisymmetric flow of hybrid nanofluid towards stretching surface. Journal of Computational Design and Engineering, 11, 146-160. https://doi.org/10.1093/jcde/qwae029.
- Rajagopal, K., Veena, P. H., & Pravin, V. K. (2006). Oscillatory motion of an electrically conducting viscoelastic fluid over a stretching sheet in a saturated porous medium with suction/blowing. Mathematical Problems in Engineering, 2006, 1-14. https://doi.org/10.115 5/MPE/2006/60560.
- Roşca, A. V., Roşca, N. C., Pop, I., & Sheremet, M. A. (2024). Natural convection and entropy generation in a trapezoidal region with hybrid nanoliquid under magnetic field. International Journal of Numerical Methods for Heat & Fluid Flow, 34, 429-450. https: //doi.org/10.1108/HFF-04-2023-0193.
- Sakkaravarthi, K., Reddy, P. B. A., & Sakthi, I. (2024). Entropy optimization in Casson tetra-hybrid nanofluid flow over a rotating disk with nonlinear thermal radiation: A Levenberg-Marquardt Neural Network approach. Journal of Computational Design and Engineering, qwae086, 333-354, https://doi.org/10.1093/jcde/qwae086.
- Saleem, S., Qasim, M., Alderremy, A., & Noreen, S. (2020). Heat transfer enhancement using different shapes of Cu nanoparticles in the flow of water based nanofluid. Physica Scripta, 95, 055209. https://doi.org/10.1088/1402-4896/ab4ffd.
- Salehi, M., Afshar, S. R., Ali, R., & Chamkha, A. J. (2023). Numerical investigation of TiO2-water nanofluid heat transfer in a porous wavy circular chamber with a <sup>⊥</sup>-shaped heater under magnetic field. Case Studies in Thermal Engineering, 49, 103405. https://doi.or g/10.1016/j.csite.2023.103405

- Sheikh, M., & Abbas, Z. (2015). Effects of thermophoresis and heat generation/absorption on MHD flow due to an oscillatory stretching sheet with chemically reactive species. Journal of Magnetism and Magnetic Materials, 396, 204-213. https://doi.org/10.1016/j.jm mm.2015.08.011.
- Sheikholeslami, M., & Bhatti, M. M. (2017). Forced convection of nanofluid in presence of constant magnetic field considering shape effects of nanoparticles. International Journal of Heat and Mass Transfer, 111, 1039-1049. https://doi.org/10.1016/j.ijheatma sstransfer.2017.04.070.
- Soomro, F. A., Rizwan-ul-Haq, K., Z., H., & Zhang, Q. (2017). Numerical study of entropy generation in MHD water-based carbon nanotubes along an inclined permeable surface. The European Physical Journal Plus, 132, 412. https://doi.org/10.1140/epjp/i2017-11667-5.
- Subramanian, K. R. V., Rao, T. N., & Balakrishnan, A. (2019). Nanofluids and Their Engineering Applications. CRC Press.
- Thumma, T., Wakif, A., & Animasaun, I. L. (2020). Generalized differential quadrature analysis of unsteady three-dimensional MHD radiating dissipative Casson fluid conveying tiny particles. Heat Transfer, 49, 2595-2626. https://doi.org/10.1002/htj.21736.
- Wakif, A., Boulahia, Z., Ali, F., Eid, M. R., & Sehaqui, R. (2018). Numerical analysis of the unsteady natural convection MHD couette nanofluid flow in the presence of thermal radiation using single and two-phase nanofluid models for Cu-Water nanofluids. International Journal of Applied and Computational Mathematics, 4, 81. https://doi.org/10.1007/s40819-018-0513-y.
- Wakif, A., Boulahia, Z., Mishra, S. R., Mehdi Rashidi, M., & Sehaqui, R. (2018). Influence of a uniform transverse magnetic field on the thermo-hydrodynamic stability in water-based nanofluids with metallic nanoparticles using the generalized Buongiorno's mathematical model. The European Physical Journal Plus, 133, 181. https: //doi.org/10.1140/epjp/i2018-12037-7.
- Wakif, A., Chamkha, A., Thumma, T., Animasaun, I. L., & Sehaqui, R. (2021). Thermal radiation and surface roughness effects on the thermo-magneto-hydrodynamic stability of alumina-copper oxide hybrid nanofluids utilizing the generalized Buongiorno's nanofluid model. Journal of Thermal Analysis and Calorimetry, 143, 1201-1220. https://doi.org/10.1007/s10973-020-09488-z.
- Wakif, A., Qasim, M., Afridi, M. I., Saleem, S., & Al-Qarni, M. M. (2019). Numerical examination of the entropic energy harvesting in a magnetohydrodynamic dissipative flow of stokes' Second problem: Utilization of the gear-generalized differential quadrature method. Journal of Non-Equilibrium Thermodynamics, 44, 385-403. https://doi.org/10.1515/jnet-2018-0099.
- Wang, C. Y. (2002). Flow due to a stretching boundary with partial slip—An exact solution of the Navier–Stokes equations. Chemical Engineering Science, 57, 3745-3747. https://doi.org/10.1016/S0009-2509(02)00267-1.
- Wang, F., Fatunmbi, E. O., Adeosun, A. T., Salawu, S. O., Animasaun, I. L., & Sarris, I. E. (2023). Comparative analysis between copper ethylene-glycol and copper-iron oxide ethylene-glycol nanoparticles both experiencing coriolis force, velocity and temperature jump. Case Studies in Thermal Engineering, 47, 103028. https://doi. org/10.1016/j.csite.2023.103028.
- Yasir, M., & Khan, M. (2024). Thermal efficiencies of ohmic cobalt ferrite and magnetite hybrid ferrofluid flow over an exponentially vertically shrinking surface. Alexandria Engineering Journal, 90, 120-128. https://doi.org/10.1016/j.aej.2024.01.055.
- Yasir, M., Khan, M., Alqahtani, A. S., & Malik, M. Y. (2023). Numerical study of axisymmetric hybrid nanofluid MgO-Ag/H2O flow with non-uniform heat source/sink. Alexandria Engineering Journal, 75, 439-446. https://doi.org/10.1016/j.aej.2023.05.062.

- Yasir, M., Malik, Z. U., Alzahrani, A. K., & Khan, M. (2023). Study of hybrid Al2O3-Cu nanomaterials on radiative flow over a stretching/shrinking cylinder: Comparative analysis. Ain Shams Engineering Journal, 14, 102070. https://doi.org/10.1016/j.asej.2022.102070.
- Zhang, K., Shah, N. A., Alshehri, M., Alkarni, S., Wakif, A., & Eldin, S. M. (2023). Water thermal enhancement in a porous medium via a suspension of hybrid nanoparticles: MHD mixed convective Falkner's-Skan flow case study. Case Studies in Thermal Engineering, 47, 103062. https://doi.org/10.1016/j.csite.2023.103062
- Zhang, L., Zhang, H., Wang, S., Song, J., Yao, X., & Wang, W. (2024). Boundary layer and entropy analysis of non-Newtonian Casson nanofluids moving nonlinearly in a wedge-shaped stretching plate under an unsteady flow. Case Studies in Thermal Engineering, 56, 104193. https://doi.org/10.1016/j.csite.2024.104193.
- Zheng, L.-C., Jin, X., Zhang, X.-X., & Zhang, J.-H. (2013). Unsteady heat and mass transfer in MHD flow over an oscillatory stretching surface with Soret and Dufour effects. Acta Mechanica Sinica, 29, 667-675. https://doi.org/10.1007/s10409-013-0066-6.